

Shock-induced plasticity in tantalum single crystals: Interatomic potentials and large-scale molecular-dynamics simulations

R. Ravelo,^{1,2,*} T. C. Germann,^{3,†} O. Guerrero,^{4,‡} Q. An,^{5,§} and B. L. Holian^{3,||}

¹*Physics Department and Materials Research Institute, University of Texas, El Paso, Texas 79968-0515, USA*

²*X-Computational Physics Division, Los Alamos National Laboratory, Los Alamos, New Mexico 87545, USA*

³*Theoretical Division, Los Alamos National Laboratory, Los Alamos, New Mexico 87545, USA*

⁴*Physics Department, University of Texas, El Paso, Texas 79968-0515, USA*

⁵*Materials and Process Simulation Center, California Institute of Technology, Pasadena, California 91125, USA*

(Received 31 May 2013; revised manuscript received 15 September 2013; published 3 October 2013)

We report on large-scale nonequilibrium molecular dynamics simulations of shock wave compression in tantalum single crystals. Two new embedded atom method interatomic potentials of Ta have been developed and optimized by fitting to experimental and density functional theory data. The potentials reproduce the isothermal equation of state of Ta up to 300 GPa. We examined the nature of the plastic deformation and elastic limits as functions of crystal orientation. Shock waves along (100), (110), and (111) exhibit elastic-plastic two-wave structures. Plastic deformation in shock compression along (110) is due primarily to the formation of twins that nucleate at the shock front. The strain-rate dependence of the flow stress is found to be orientation dependent, with (110) shocks exhibiting the weaker dependence. Premelting at a temperature much below that of thermodynamic melting at the shock front is observed in all three directions for shock pressures above about 180 GPa.

DOI: [10.1103/PhysRevB.88.134101](https://doi.org/10.1103/PhysRevB.88.134101)

PACS number(s): 02.70.Ns, 61.50.Ks, 62.50.Ef, 64.10.+h

I. INTRODUCTION

Tantalum is a body-centered-cubic (bcc) transition metal with no confirmed experimentally observed solid-solid phase changes with pressure or temperature. Due to its high melting temperature and strength, it is widely used in the production of high-temperature superalloys for many technological applications. Its simple phase diagram at high pressures makes it an ideal pressure standard. A transition from bcc to an ω (hexagonal) phase has been reported in experiments of Ta shocked to 45 GPa.¹ However, diamond-anvil cell (DAC) experiments and *ab initio* calculations of the zero-temperature ($T = 0$) equation of state (EOS) place bcc as the most stable phase over a wide range of pressures. Recent quantum molecular dynamics (QMD) simulations of the melt curve of Ta suggest that for pressures above about 100 GPa, Ta may undergo a phase transition to a hex- ω phase, and the phase diagram of Ta may exhibit a bcc/hex- ω /liquid triple point located around 100 GPa and 250 OK.² However, the conclusions drawn from these QMD simulations and the existence of a phase change in Ta at high pressure have been questioned recently by Haskins *et al.*,³ who argue that the small system sizes associated with the QMD simulations may overestimate the stability of the ω phase relative to the bcc one. The existence of a phase transition (such as the postulated bcc \rightarrow hex- ω one) at high pressures and temperatures has also been proposed as a way to explain marked differences in the melt line between DAC and shock-wave experiments.⁴⁻⁷ However, so far no direct evidence of a high-pressure phase transition in Ta has been reported in DAC experiments. A non-equilibrium phase transformation in the shock experiments has been proposed as a plausible explanation for the experimentally observed transition at low pressures.⁸ These issues underscore some of the current controversies regarding the high-temperature/high-pressure properties of this system. Surprisingly, while there have been many computational studies of the thermal and mechanical properties of Ta at high pressures,⁹⁻¹¹ there has not

been, to date, a systematic atomistic simulation study of the dynamical response of Ta to shock-wave and high strain-rate loading.

The main purpose of this work is to investigate via atomistic simulations the dynamical response of Ta single crystals to high strain-rate deformation and shock-wave propagation. The large majority of non-equilibrium molecular-dynamics (NEMD) studies of shock-induced plasticity and defect nucleation have dealt with face-centered-cubic (fcc) metals. These studies have revealed that the elastic-plastic transition in defect-free single crystals is characterized by high elastic limits and directional anisotropies which show marked differences in the morphology of defects: partial dislocation loop nucleation is the main deformation mechanism for shock-wave propagation along the (100) direction, and full loop nucleation and multiplication is the main mechanism for shock propagation along the (110) and (111) directions.^{12,13} Less is known about shock-induced plasticity in monocrystalline bcc metals,¹⁴ bcc metals that belong to the groups V and VI of the periodic table, such as Ta, exhibit interesting mechanical features which include a strong orientation, temperature, and strain-rate dependence in the yield stress. Some of these peculiar properties are due to the screw dislocation core structure¹⁵ and an unusual slip activation system which exhibit a marked dependence on temperature and orientation (slip asymmetry).¹⁶

We have employed large-scale NEMD simulations to study the characteristics of shock-wave propagation along the low-index directions (100), (110), and (111). The Hugoniot elastic limit (HEL), plastic deformation mechanisms, and corresponding anisotropies in shock-wave structure were examined along these three low-index crystal orientations for pressures up to 300 GPa. We find that twin formation is the main mechanism of stress relief at the shock front for propagation along the (110) direction, while very little twinning is observed in the shock-induced plasticity of Ta along (100).

Many semi-empirical interatomic potential models of Ta have been developed over the years. They include the embedded atom method (EAM),^{17,18} Finnis-Sinclair (FS),^{19–22} modified embedded atom method (MEAM),²³ angular-dependent potential (ADP)²⁴ and model generalized pseudopotential theory (MGPT) potentials,²⁵ among others. Of these, the MGPT potential provides the most accurate description of Ta over a wider pressure-temperature range. However, the inherent volume dependence of the MGPT potential makes it difficult to implement in dynamical studies of shock-wave phenomena, and the computational expense of MGPT is significantly greater than the others. In this work, we construct two new EAM interatomic potentials for Ta by fitting to an experimental and first-principles database that includes selected high-pressure data. Among the interatomic potential models employed in the description of metallic systems, the EAM is among the most popular, particularly in large-scale atomistic simulations. It provides a good description of the many-body cohesion in metals and their mechanical properties, at a low computational cost. There is no reason to expect, however, that a model like the EAM which assumes a spherically symmetric electron density can accurately reproduce the mechanical properties of bcc transition metals, given the directional bonding associated with the partially filled d bands. We will show that by carefully selecting high pressure properties in the training set, EAM can provide a reasonable description of bcc Ta over a much larger pressure range than in models which employ mostly zero-pressure and -temperature properties, even if the fitting database includes energy differences of various phases at equilibrium volumes.

The organization of the paper is as follows: In the next section we detail the method employed in the development of the EAM interatomic potentials, the *ab initio* and experimental database used in the fitting procedure, functional forms, and the parametrization scheme. We also compare selected mechanical properties of Ta from both experimental measurements and density functional theory (DFT) calculations with the corresponding EAM models' predictions. In Sec. III we describe the equilibrium and nonequilibrium simulation methods and the computational geometries. Simulation results are presented in Sec. IV, and in Sec. V we provide our summary and conclusions.

II. POTENTIAL DEVELOPMENT

In this section we detail our approach to constructing EAM interatomic potentials for high-pressure applications. Most of the Ta potential models in the literature based on either EAM or FS parametrization schemes^{17–22} were not specifically developed for high-pressure/high-temperature applications. As a result, high-pressure properties are reproduced with various degrees of success. Since Ta has no confirmed solid-solid phase changes with pressure, one criterion we employed in testing the transferability of the models was the stability of the bcc phase with respect to other energetically close phases. The stability of the bcc phase against other phases was incorporated in the fitting scheme as a discriminant in the acceptance/rejection of the parameter sets generated in the optimization procedure. The goal was to develop a new EAM Ta model potential which would exhibit no phase

changes within a pressure range of relevance in shock-wave simulations and be relatively short-ranged, so that it can be used in large-scale atomistic simulations requiring fast energy and force evaluations.

A. First-principles calculations

A $T = 0$ database of Ta properties was calculated within the framework of DFT using the Vienna Ab initio Simulation Package (VASP).²⁶ The DFT calculations included structural energies, elastic constants, stress tensor as a function of compression along the low-index crystallographic orientations, twin/antitwin energies, and generalized stacking fault (GSF) energies. The projector-augmented wave (PAW) method²⁷ was used to treat the ion-electron interaction. A plane-wave cutoff energy of 600 eV was found to give sufficiently accurate structural energies and converged stresses and, unless noted, was used in most calculations. We employed the generalized gradient approximation (GGA) with the Perdew-Wang 91 functional,²⁸ the PAW potential with $5p$ electrons as valence, and neglected spin-orbit coupling. (Previous *ab initio* studies of the equation of state of Ta have shown a negligible contribution to the energy from spin-orbit interactions.^{29,30}) The integration over the Brillouin zone was performed using the Monkhorst-Pack (MP) scheme.³¹ Most total-energy and stress-strain calculations were carried out using a $17 \times 17 \times 17$ MP k -point grid. The unrelaxed gamma surface (GS) calculations utilized supercells containing 12 atomic layers with 12 and 24 atoms, for the $\{112\}$ and $\{110\}$ GS, respectively, using a $15 \times 15 \times 1$ MP k -point mesh. The stress-strain relations were computed for volumetric as well as uniaxial deformations along the (100), (110), and (111) crystallographic directions.

B. EAM potential functions and parametrization

The embedded atom method (EAM)³² is semiempirical, based on DFT, in which the total energy of any configuration of nuclei can be expressed as a unique functional of the total electron density. The total energy of the system can be written as a sum over atomic energies E_i :

$$E_{\text{tot}} = \sum_i^N E_i. \quad (1)$$

The energy per atom E_i is given by

$$E_i = F(\bar{\rho}_i) + \frac{1}{2} \sum_j \phi(r_{ij}), \quad (2)$$

where $\phi(r_{ij})$ is a pairwise, spherically symmetric interaction potential between atom i and neighbor atom j at a radial distance r_{ij} . $F(\bar{\rho}_i)$ is the so-called embedding energy contribution, which is a nonlinear function of the electron density $\bar{\rho}_i$ at site i , assumed to be directly proportional to the atomic density surrounding the site, expressed as a sum over all neighboring atoms weighted by a pairwise, spherically symmetric function w :

$$\bar{\rho}_i = \sum_{j \neq i} w(r_{ij}). \quad (3)$$

Two EAM potentials, referred to here as Ta1 and Ta2, were constructed by employing a parametrization procedure similar

to that outlined in Ref. 33 and modified here to introduce high-pressure properties into the fitting procedure. In this prescription, the cold curve (i.e., the $T = 0$ EOS, E_{EOS}) of the solid, as a function of volume V (lattice constant a) for the equilibrium structure (which, for Ta at zero pressure, is bcc), determines the embedding function $F(\bar{\rho})$:

$$F(\bar{\rho}) = E_{\text{EOS}}(a) - \frac{1}{2} \sum_{j \neq i} \phi(r_{ij}). \quad (4)$$

The cold curve for Ta was evaluated from DFT calculations and fitted to a Rydberg function³⁴ in the form proposed by Rose *et al.*,³⁵ extended here to include higher-order (cubic and quartic) terms:

$$E_{\text{EOS}}(a^*) = -E_c(1 + a^* + f_3 a^{*3} + f_4 a^{*4})e^{-a^*}. \quad (5)$$

The dimensionless parameter $a^* = \alpha(a/a_0 - 1)$ is proportional to the linear strain, and $\alpha = \sqrt{(9B_0V_0)/E_c}$ is a dimensionless measure of the anharmonic repulsive strength. The $P = T = 0$ constants are the lattice constant a_0 (obtained from the equilibrium volume V_0), the cohesive energy E_c , and the bulk modulus B_0 .

The DFT binding energy data of the bcc structure was shifted to make the minimum of the energy curve coincide with the experimental cohesive energy of Ta ($E_0 = -8.10$ eV/atom). The DFT data was also scaled [a^* in Eq. (5)] by the experimental equilibrium value of the lattice constant of Ta, $a_0 = 3.304$ Å. The cubic and quartic coefficients f_3 and f_4 , while usually taken to be zero in low-pressure applications, become important at high compressions. The value of the cubic coefficient f_3 can be related to the thermal expansion coefficient, which is proportional to the Grüneisen parameter,³⁶ and also to the pressure derivative of the bulk modulus (evaluated at zero pressure and temperature, $B'_0 = (dB/dP)_{P=T=0}$):

$$f_3 = \frac{1}{2\alpha}(B'_0 - 1) - \frac{1}{3}. \quad (6)$$

The pairwise interaction in Eq. (2) was chosen to be a modified Rydberg function on the repulsive side and a short-range polynomial on the attractive side. While not rigorous, this form assumes that as a function of compression, the ion-repulsion at short distances is dominated by the pairwise interactions. Therefore, with dimensionless distance parameter $r^* = \alpha_p(r/r_1 - 1)$, analogous to a^* in Eq. (5), the pairwise interaction ϕ is given by

$$\phi(r) = \begin{cases} U_0(1 + r^* + \beta_3 r^{*3} + \beta_4 r^{*4})e^{-r^*} & (0 \leq r \leq r_s), \\ U_0(r - r_c)^s \sum_{i=1}^4 a_i (r - r_c)^{i-1} & (r_s \leq r \leq r_c), \\ 0 & (r > r_c), \end{cases} \quad (7)$$

where $r_1, r_s, r_c, s, \alpha_p, U_0, \beta_3$, and β_4 are fitting parameters. The coefficients a_i in Eq. (7) are uniquely determined by matching the Rydberg and polynomial functions, and their first, second, and third derivatives at $r = r_s$.

Finally, the electron density function $w(r)$ in Eq. (3) was taken to be a simple continuous function similar to one previously used in the construction of a generic analytical EAM model employed in the study of high-stress plastic

deformation in metals:³⁷

$$w(r) = \begin{cases} \rho_0 \left[\frac{(r_c^p - r^p)}{(r_c^p - r_0^p)} \right]^q & (0 \leq r \leq r_c), \\ 0 & (r > r_c), \end{cases} \quad (8)$$

where r_0 is the equilibrium nearest-neighbor distance at $P = T = 0$. The analytical function $w(r)$ behaves qualitatively like a Gaussian and smoothly goes to zero at the cutoff distance r_c . The arbitrary constant ρ_0 is determined from the normalization of $\bar{\rho}$ in Eq. (3) and p, q , and r_c are fitting parameters.

While the Ta1 and Ta2 models share the same functional forms, the number of fitting parameters in the two models is different. In the optimization of the Ta1 model, the parameters β_3 and β_4 were set to zero, and the spline point r_s was fixed to be the minimum of the pair potential ($r_s = r_1$). This reduces the number of fitting parameters in the Ta1 model to 7, while there are 10 in the Ta2 model. The training sets used in the optimization of the fitting parameters included the experimental values of the elastic constants, vacancy formation energy and Grüneisen parameter, as well as properties obtained from DFT calculations, such as the stress tensor as a function of uniaxial compression along the (100) orientation, unrelaxed (100) surface energy, and the unstable stacking fault energy of the $\{112\}\langle\bar{1}\bar{1}1\rangle$ section of the gamma surface. An important step in the optimization of the model parameters was the evaluation of the $T = 0$ enthalpy difference between bcc and other energetically close crystallographic phases [primarily hexagonal close packed (hcp), fcc, and A15] as a function of compression. Each iterative model was tested for “artificial” phase transitions at $T = 0$ within a prespecified pressure range, the smallest of which was arbitrarily set to 0–300 GPa. If from the enthalpy difference, the model potential exhibited a phase transition within this pressure range, the parameter set was discarded and a new iterative random search was started. The lowest transition pressure cutoff of 300 GPa, was chosen close to the value of the solid-liquid transition pressure along the principal Hugoniot, about 290 GPa.³⁸ While checking for phase transitions based on enthalpy differences is computationally intensive and adds a layer of complexity to the optimization of the model’s fitting parameters, we believe it is a necessary step for generating interatomic potentials with the correct phase stability in the desired pressure range. It is also an important check of the transferability of interatomic potentials for bcc metals based on the EAM or the FS formalisms, since those models have a tendency to undergo a bcc \rightarrow hcp transition with compression. A simulated-annealing, global-optimization method³⁹ was employed in the fitting of the models to selected target values in the training sets. Checks for artificial phase transitions within a minimum cutoff transition pressure of 300 GPa were used as a discriminant of the transferability of the model. Parameter sets not meeting this check were discarded regardless of how well they reproduce all other properties in the training set. The two EAM models reported in this work required several post-optimization iterations to meet this condition: 13 for Ta1 and 19 for Ta2. In Table I we list the parameter values of the Ta1 and Ta2 EAM models, and Fig. 1 shows the potential functions $\phi(r)$, $w(r)$, and $F(\bar{\rho})$ for both models.

TABLE I. Parameters of the EAM functions of the Ta1 and Ta2 potentials.

Parameter	Ta1	Ta2
E_c (eV)	8.1	8.1
α	4.934	4.950
a_0 (Å)	3.304	3.304
f_3	0.0	-0.035744
f_4	0.0	-0.020879
U_0 (eV)	0.80	1.1094
r_1 (Å)	2.860	2.7826
α_p	4.70	4.6463
β_3	0.0	0.160
β_4	0.0	0.060
r_s (Å)	2.86	2.8683
s	7.50	8.00
r_c (Å)	5.30	5.5819
a_1 (Å ^{-s})	-0.11745	-0.039742
a_2 (Å ^{-(s+1)})	0.12309	0.038568
a_3 (Å ^{-(s+2)})	-0.043904	-0.012714
a_4 (Å ^{-(s+3)})	0.0053178	0.0014196
p	4.0	5.9913
q	4.0	8.0
ρ_0	0.077723	0.074870

C. Evaluations of the Potentials

In Table II we list some mechanical properties of bcc Ta evaluated with the EAM potentials along with corresponding experimental values and values from DFT calculations. By construction, the models reproduce the target values of the lattice constant (a_0), cohesive energy (E_{coh}), and bulk modulus at zero pressure (B_0), as well as reproducing the DFT-calculated cold curve (Fig. 2) used in the fit to Eq. (5). The calculated pressure-volume relation is shown in Fig. 3, compared with DFT and experimental diamond-anvil cell (DAC) measurements.^{40,43} The agreement with the DFT data is a result of fitting to the DFT EOS (Fig. 2). The deviation of DFT from the DAC data in the pressure-volume relation (Fig. 3) can be explained from DFT's higher value of B'_0 ; similarly, a linear fit to shock data⁵⁴ gives a higher value than DAC data, namely, $B'_0 = 4.1$.

The stress-strain relations are a measure of how well the EAM potentials perform beyond linear elasticity, namely, reproducing the third- and higher-order elastic constants. These relations are also important in shock physics simulations because they represent how well an interatomic potential model reproduces the pressure dependence of the sound velocities. The computed stress-strain relations as a function of uniaxial compression along the $\langle 100 \rangle$, $\langle 110 \rangle$, and $\langle 111 \rangle$ low-index directions are shown in Fig. 4 and compared with corresponding DFT calculated values. Given that the DFT values of the $\langle 100 \rangle$ stresses P_{xx} and P_{zz} at 20% compression were the only stress values included in the training set, both EAM potential models reproduce reasonably well the anisotropy of the stress-strain relations under compression.

As already mentioned, we incorporated into the fitting procedure the enthalpy difference ΔH at zero temperature between the bcc phase and other energetically close phases. ΔH was used to check for possible artificial phase transitions

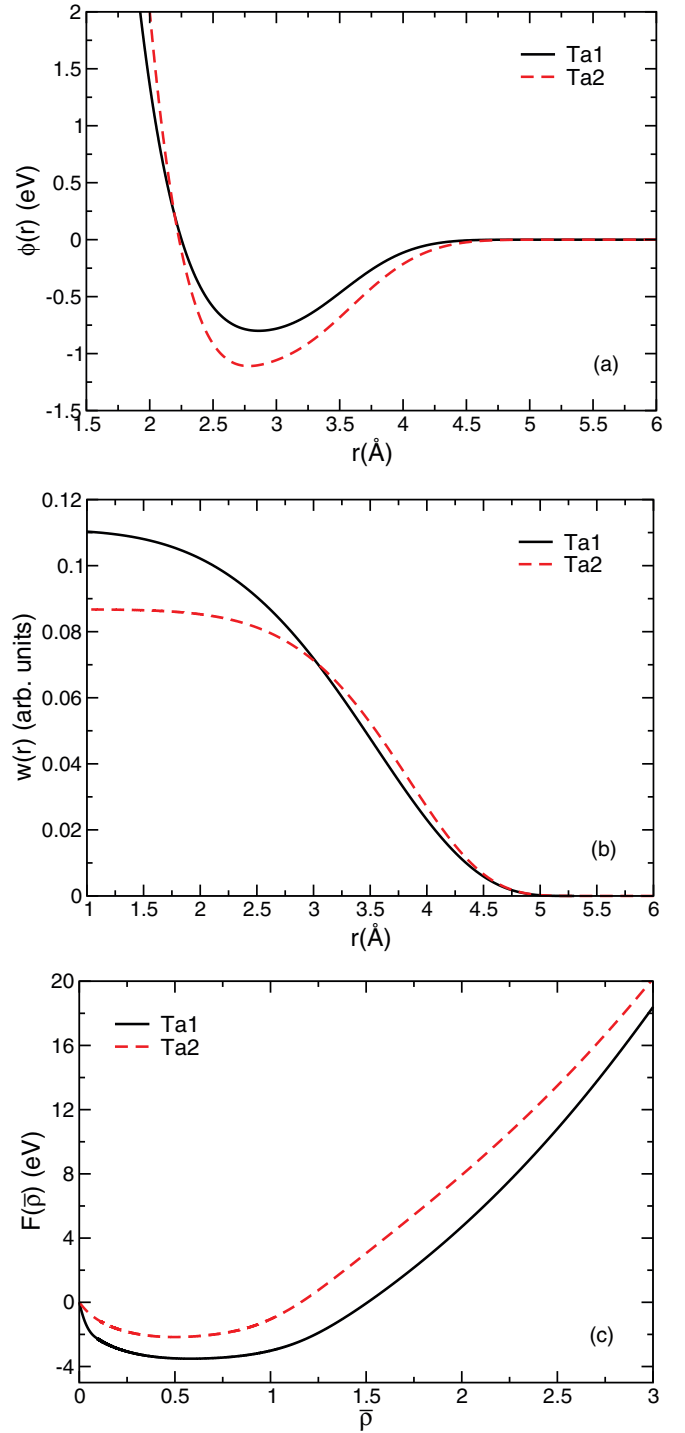


FIG. 1. (Color online) Potential functions of the EAM models Ta1 and Ta2: (a) pair interaction potential Eq. (7); (b) electron density $w(r)$ Eq. (8); (c) embedding function $F(\bar{\rho})$.

within a reasonable pressure range. This step we believe is necessary in the optimization of EAM model potentials for high pressure applications, particularly since the EAM and FS schemes can exhibit “unwanted” phase transition with compression, usually to ideal hcp. Illustrating this point, Fig. 5 shows the enthalpy difference between bcc and ideal hcp Ta as a function of pressure for several EAM and FS interatomic potentials of Ta in the literature, as well as for the present EAM

TABLE II. Selected properties of Ta calculated with the EAM potentials Ta1 and Ta2, compared with experimental and DFT data. Unless otherwise noted, DFT values are from this work. Notations are explained in the text.

Quantity	Ta1	Ta2	Experiment	DFT
a_0 (Å)	3.304	3.304	3.304 ^a	3.321
E_{coh} (eV/atom)	-8.100	-8.100	-8.100 ^b	-8.216
C_{11} (GPa)	263	267	264 ^c	247
C_{12} (GPa)	161	160	160 ^c	170
C_{44} (GPa)	82	86	82 ^c	67
B'_0	4.1	3.9	3.25 ^a , 3.4 ^d	3.95, 4.3 ^f
E_v^f (eV)	2.43	2.00	2.8 ± 0.6 ^g	2.99 ^h
E_v^m (eV)	0.99	1.08	0.7 ⁱ	0.83 ^h
γ_{100} (J/m ²)	2.28	2.40	2.90 ^j	2.27 ^k
γ_{110} (J/m ²)	1.97	2.04	2.90 ^j	2.31 ^k
γ_{111} (J/m ²)	2.53	2.74	2.90 ^j	2.74 ^k
$\gamma_{\text{us}}\{211\}\langle 111 \rangle$ (J/m ²)	1.017	0.975	—	1.000
$\gamma_{\text{us}}\{110\}\langle 111 \rangle$ (J/m ²)	0.864	0.803	—	0.840
$\gamma_{\text{us}}\{110\}\langle 001 \rangle$ (J/m ²)	2.194	2.208	—	1.951
T_m (K)	3033	3080	3280 ^l	3270 ^m
α_L (300 K) ($\times 10^{-6}$ K ⁻¹)	2.63	4.24	6.5 ⁿ	8.8 ^o
γ_{th}	0.65 ^p	1.04 ^p	1.64 ^q	2.28 ^m

^aReference 40.

^bReference 41.

^cReference 42.

^dReference 43.

^eReference 40.

^fReference 44.

^gReference 45.

^hReference 46.

ⁱReference 47.

^jAverage orientation, extrapolated to 0 K (Ref. 48).

^kReference 49.

^lReference 50.

^mReference 29.

ⁿReference 51.

^oReference 52.

^pFrom molecular dynamics simulations at 300 K and zero pressure.

^qReference 53.

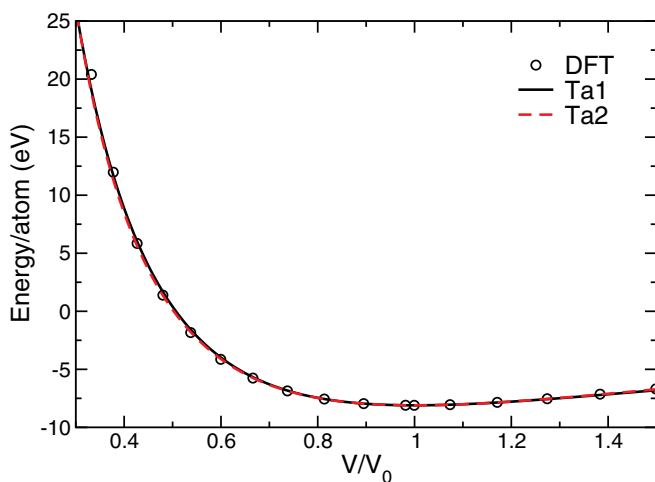


FIG. 2. (Color online) Equation of state at $T = 0$ of bcc Ta evaluated with the EAM potentials and from DFT calculations (open circles).

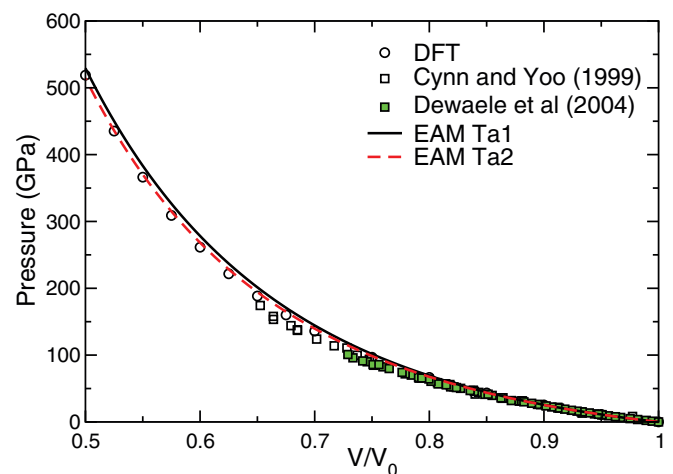


FIG. 3. (Color online) Pressure vs volume at $T = 0$ for bcc Ta calculated with the EAM models compared with DFT data (open circles) and DAC experimental data: open squares, Ref. 43; filled squares, Ref. 40.

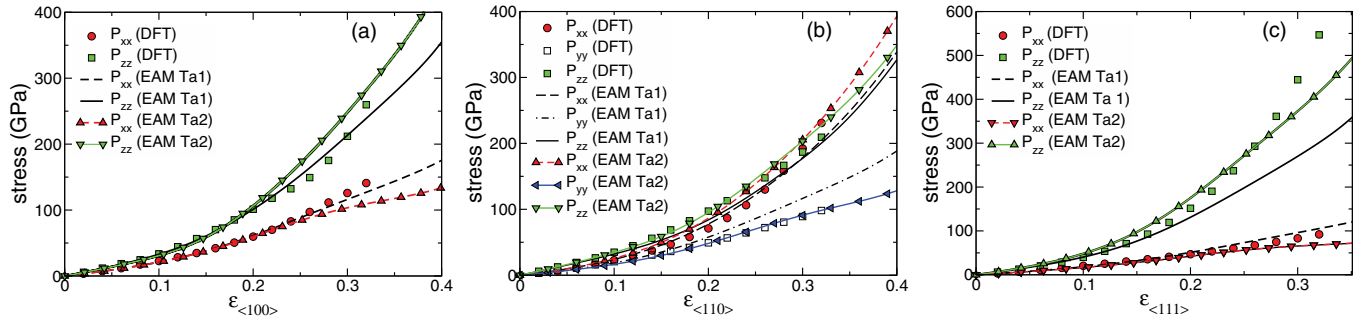


FIG. 4. (Color online) Stress tensor as a function of uniaxial compressive strain evaluated with the EAM models and compared with corresponding values from DFT calculations along crystal directions: (a) $\langle 100 \rangle$, (b) $\langle 110 \rangle$, and (c) $\langle 111 \rangle$.

Ta1 and Ta2 models. From $\Delta H = 0$, the Ta1 model undergoes a bcc \rightarrow hcp transition at $P = 463$ GPa and the Ta2 model at $P = 325$ GPa. These values place an upper pressure limit on the applicability of these potentials in high-pressure studies of Ta. We should note that most of the potentials shown in Fig. 5 perform as expected in the pressure range for which they were optimized.

1. Defect energies and thermal properties

The vacancy formation energy E_v^f for Ta is underestimated by both models with respect to the experimental and DFT calculations. While the EAM Ta1 value of 2.43 eV is within the experimental error (2.8 ± 0.6), the Ta2 calculated value is significantly lower (2.0 eV). The vacancy migration energy E_v^m is overestimated by the models, but in reasonable agreement with DFT calculations. Both models however, are expected to predict lower activation energies of self-diffusion of vacancies.

This is not a deficiency of the model as much as a compromise in relative weights given to low- and high-pressure properties.

The relaxed surface energies ($\gamma_{100}, \gamma_{110}, \gamma_{111}$) are in reasonable agreement with DFT calculations, and the average DFT value of 2.4 J/m^2 matches well with the average EAM values of 2.3 and 2.4 J/m^2 for the Ta1 and Ta2 models, respectively. The experimental value of 2.9 J/m^2 listed in Table II is an extrapolated value to $T = 0$. The measured experimental value, at or near T_{melt} , is 2.49 J/m^2 .⁴⁸

How best to include thermal properties in the optimization of interatomic potentials is an issue which we explored in some depth, since it is not common practice to fit to them. While the pressure derivative of the bulk modulus accounts for the mechanical anharmonicity in the $T = 0$ EOS, a straightforward approach in the optimization procedure that should help to account for thermal anharmonic properties, such as the thermal expansion coefficient and the thermal contribution to the pressure, is to fit to the Grüneisen parameter, whose thermodynamic definition is

$$\gamma_{\text{th}} = V \left. \frac{\partial P}{\partial E} \right|_V = \frac{V}{C_V} \left. \frac{\partial P}{\partial T} \right|_V = \frac{\alpha_V B_T V}{C_V}, \quad (9)$$

where P is the pressure, E the internal energy, $\alpha_V = (1/V)(\partial V/\partial T)_P$ is the volumetric thermal expansion coefficient, B_T is the isothermal bulk modulus, and C_V is the constant-volume heat capacity. From equilibrium MD simulations of both pressure vs temperature at constant volume, and volume vs temperature at constant pressure, we verified that the relationship between γ_{th} and α_V in Eq. (9) is correct to about 1%, including the classical limit of the heat capacity per atom, $C_V = 3k_B$.

The vibrational Grüneisen parameter γ_{vib} is a microscopic, low-temperature, quantum-mechanical approximation to γ_{th} , assuming that quasiharmonic lattice dynamics is appropriate, and the normal-mode frequencies $\omega_{n,\mathbf{k}}(V)$ depend only on volume, not temperature:

$$\gamma_{\text{vib}}(V, T) = \frac{\sum_{n,\mathbf{k}} \gamma_{n,\mathbf{k}}(V) c_{n,\mathbf{k}}(V, T)}{\sum_{n,\mathbf{k}} c_{n,\mathbf{k}}(V, T)}, \quad (10)$$

where

$$\gamma_{n,\mathbf{k}}(V) = - \frac{\partial [\ln \omega_{n,\mathbf{k}}(V)]}{\partial (\ln V)} \quad (11)$$

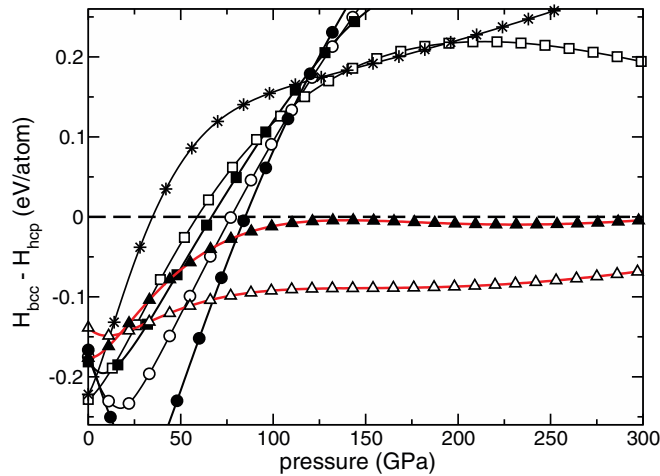


FIG. 5. (Color online) Enthalpy difference at $T = 0$ between the bcc and ideal hcp crystal phases as a function of pressure for the Ta1 and Ta2 potential models compared with various other interatomic potentials for Ta in the literature. Open circles (\circ): FS model of Ackland and Thetford;²⁰ open square (\square): EAM model of Johnson and Oh;¹⁷ solid circles (\bullet): EAM model of Guellil and Adams;¹⁸ solid squares (\blacksquare) FS model of Dai *et al.*;²¹ stars ($*$): FS potential of Liu *et al.*;²² open triangles (\triangle): EAM Ta1 model; solid triangles (\blacktriangle): EAM Ta2 model. The Ta1 model crosses the $\Delta H = 0$ line at $P = 463$ GPa and the Ta2 model at $P = 325$ GPa.

is the normal-mode Grüneisen parameter, and $c_{n,\mathbf{k}}(V, T)$ is the normal-mode (\mathbf{k}, n) contribution to the specific heat:

$$c_{n,\mathbf{k}}(V, T) = \left[\frac{\hbar\omega_{n,\mathbf{k}}(V)}{k_B T} \right]^2 \frac{e^{\hbar\omega_{n,\mathbf{k}}(V)/k_B T}}{[e^{\hbar\omega_{n,\mathbf{k}}(V)/k_B T} - 1]^2} \quad (12)$$

where \mathbf{k} is the wave vector and n is the branch index (polarization). The summation over the normal modes spans the first Brillouin zone. When the temperature T is much higher than $\hbar\omega_{\max}(V)/k_B T$, then the heat capacity is the classical limit, $C_V = 3Nk_B$ (N is the number of atoms/unit cell), where all normal modes are fully thermally populated; the Grüneisen parameter is then simply the average value of the normal-mode Grüneisen parameters $\gamma_{n,\mathbf{k}}(V)$. At lower temperatures, the lower-frequency modes can dominate the quantum average in Eq. (10), so that the Grüneisen parameter can differ noticeably from the high-temperature (or $\hbar = 0$) classical limiting value. It should also be noted that there is no guarantee that the phonon Grüneisen parameter γ_{vib} will correspond to the experimental thermodynamic Grüneisen parameter γ_{th} in Eq. (9), particularly if the quasiharmonic approximation (QHA) does not hold.

Several approximate, macroscopic models of γ_{th} have been developed over the years, based on volume derivatives of the cold curve. The Dugdale-MacDonald model γ_{DM} fits a wide spectrum of elements in the periodic table and is simply related to B'_0 at $P = T = 0$:⁵⁵

$$\gamma_{\text{DM}} = \frac{1}{2}(B'_0 - 1). \quad (13)$$

(Note that γ_{DM} , which is directly proportional to the thermal expansion coefficient α_V , goes to zero for a purely harmonic three-dimensional system, as it should; other model formulations for the Grüneisen parameter do not.) While simple approximations, like γ_{DM} in Eq. (13), which is based on the cold curve via the pressure derivative of the bulk modulus, are known to have limitations,⁵⁶ less is known about how well the vibrational Grüneisen parameter γ_{vib} in Eq. (10) estimates the thermodynamic γ_{th} in Eq. (9), and hence how accurately the thermal expansion can be calculated within the quasiharmonic approximation (QHA).

A major difference in our construction of the two EAM models was the inclusion of $\gamma_{\text{DM}} = \gamma_{\text{th}}(\text{expt.}) = 1.6 \pm 0.2$ in the fitting of Ta1 (which is consistent with a value of $B'_0 = 4.2$), while we targeted a value of $\gamma_{\text{vib}} = \gamma_{\text{th}}(\text{expt.}) = 1.6 \pm 0.2$ in the training set for Ta2. While each EAM potential reproduces its intended target value of the Grüneisen coefficient, the true thermodynamic value γ_{th} (and therefore, also the linear thermal expansion coefficient $\alpha_L = \alpha_V/3$), as measured by equilibrium MD simulations, is underestimated by both EAM models, particularly by Ta1 (see Table II).

For Ta, DFT calculations overestimate the thermal expansion α_L by 35%.^{29,52} On the other hand, we see that the Ta2 EAM model *underestimates* α_L by 35%, even though the experimental value was the target (on the other hand, Ta1 underestimates α_L by 60%). The difference between the equilibrium MD and the QHA results can be associated with thermal anharmonicity. In the quasiharmonic phonon approximation, the mode Grüneisen parameter $\gamma_i = -\partial \ln \omega_i / \partial \ln V|_T$ includes the isothermal volume-dependent contribution. The isochoric anharmonic contribution $a_i = \partial \ln \omega_i / \partial T|_V$ is not treated

within QHA, which assumes all frequencies are temperature independent. These results suggest that temperature is an important factor in the vibrational anharmonicity of tantalum, with DFT calculations of the Grüneisen parameter within QHA giving values higher than those obtained from quantum molecular dynamics (QMD) simulations.⁵⁷ This is also the trend we find in the two EAM models Ta1 and Ta2 presented here.

The melt temperature at zero pressure was evaluated employing solid-liquid coexistence simulations⁵⁸ with atomic slabs comprising 16 000 atoms and periodic boundary conditions (PBC). Both models reproduce the experimental melt temperature (3280 K) within 6% (3033 K for Ta1 and 3080 K for Ta2). The enthalpy of melting is 0.26 eV/atom and 0.24 eV/atom for the Ta1 and Ta2 EAM models, respectively, compared to the experimental value of 0.325 eV/atom⁵⁹).

2. Twinning path and gamma surfaces

The ideal shear strength for bcc materials has long been associated with the maximum stress required to homogeneously shear the crystal along the twinning path⁶⁰ in which $\{112\}$ planes are sheared along the $(\bar{1}\bar{1}1)$ direction. A shear in the opposite direction also produces a twinned crystal, but with a different energy barrier. This asymmetry in the direction of shearing is characteristic of the twinning/antitwinning path in bcc lattices. The maximum slope of the one-dimensional energy surface along the twinning path is associated with the ideal (theoretical) shear stress. The total energy along the twinning/antitwinning path can be calculated by translating the primitive lattice vectors of the original bcc lattice to that of a sheared crystal with basis vectors.⁶⁰

$$\begin{aligned} \mathbf{a} &= \frac{1}{2}[\bar{1}\bar{1}1] + \frac{s}{\sqrt{18}}[\bar{1}\bar{1}1], \\ \mathbf{b} &= \frac{1}{2}[1\bar{1}1] + \frac{s}{\sqrt{18}}[\bar{1}\bar{1}1], \\ \mathbf{c} &= \frac{1}{2}[11\bar{1}]. \end{aligned}$$

In the twinning direction $0 \leq s \leq 1/\sqrt{2}$ and in the antitwinning direction, $-\sqrt{2} \leq s \leq 0$. Figure 6 shows results of

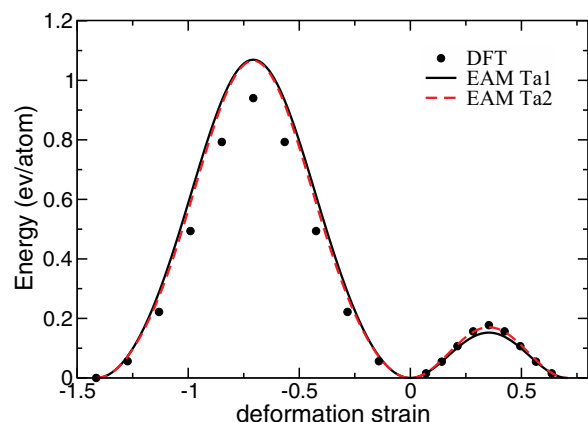


FIG. 6. (Color online) Energy as a function of strain for affine deformations along the twinning and antitwinning paths calculated with the EAM models and DFT (filled circles).

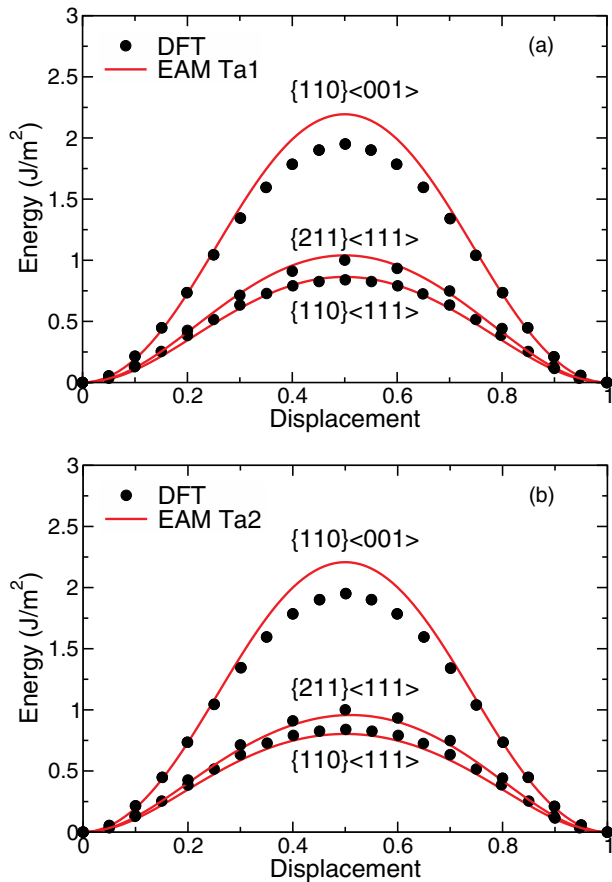


FIG. 7. (Color online) High-symmetry cross sections of the gamma surface of Ta computed using the EAM Ta potentials and DFT: (a) EAM Ta1; (b) EAM Ta2.

the unrelaxed energy along the twinning/antitwinning path calculated with the EAM Ta1 and Ta2 models and with DFT. The EAM models overestimate the energy barrier on the antitwinning path but the quantitative agreement for deformation twinning is very good. The unrelaxed energy maximum along this path is 0.177 eV from DFT calculations, while the EAM potentials give 0.15 eV and 0.17 eV for the Ta1 and Ta2 models, respectively.

Another property which is important to test for and of importance in modeling the behavior of screw dislocations is the generalized stacking-fault energy, or γ surface. Figure 7 shows high-symmetry cross sections in the $\{112\}$ and $\{110\}\gamma$ surfaces of Ta calculated with DFT and with the EAM interatomic potentials. The displacements along the shown directions are normalized by the lattice periodicity along the corresponding direction. The maxima in these curves are the unstable stacking-fault energies γ_{us} , whose values are given in Table II. The agreement overall is quantitatively good and should be taken as a first measure of how well these potentials are expected to reproduce screw dislocation core energies and their structure in Ta.

Overall, both EAM Ta potentials are equally accurate when it comes to reproducing the EOS and mechanical properties, such as elastic constants and stress-strain relations as functions of orientation. There is little or no difference between them on how well they describe the deformation energy along

the twinning/antitwinning path as well as selected symmetry cross sections of the gamma surface. This leads us to believe that they will do equally well in describing plasticity in Ta and screw dislocation core energies. The Ta1 model does better than the Ta2 model in reproducing the energetics of lattice defects but worse regarding thermal expansion and thermal pressure at high temperatures, with the Ta1 model underestimating the thermal expansion coefficient by almost 1/3 of the experimental value. This is due to the different criteria used to fit to the Grüneisen parameter in both models.

III. SHOCK COMPRESSION SIMULATIONS

Shock compression was studied via large-scale (multi-million atom) non-equilibrium molecular dynamics (NEMD) and constant-stress Hugoniot⁶¹ simulations. The atomic interactions were described by the EAM model potentials detailed in the previous section. The large-scale NEMD simulations were done with the Los Alamos National Laboratory massively parallel MD code SPASM⁶² for system sizes comprising up to 383 million atoms. The procedure we employed to initiate a shock wave of a given strength follows the method outlined in Ref. 63, and modified here to reduce heating at the impact surface. The targets consisted of rectangular slabs with cross sections between (33 nm \times 33 nm) and (132 nm \times 132 nm) and up to 1000 nm long. Periodic boundary conditions were imposed in the transverse (x and y) directions and free boundaries in the longitudinal (shock) direction, taken here to be along the z direction. The initial temperature of the Ta samples was set to 300 K. The velocity of the crystal slabs were linearly ramped from rest to a final velocity u_p in 5–10 ps, in order to minimize heating near the impact surface. Immediately after, the slabs impacted an infinitely massive piston at a velocity $-u_p$. The impact produces a shock wave that propagates away from the piston at a shock velocity $u_s - u_p$ in the frame of the moving slab. We examined piston velocities in the 500–2500 m/s range. We also carried out many more constant-stress Hugoniot⁶¹ simulations with smaller system sizes in order to probe longer time scales and sample more points along the Hugoniot. The Hugoniot simulation samples were comprised of up to 100 000 atoms arranged approximately in a cube. The uniaxial compression was applied along the low-index crystallographic directions (100), (110), and (111), and the strain rate was selected to approximate the rise times of the shock profiles in the NEMD simulations, typically 10^{10} – 10^{11} s⁻¹.

IV. RESULTS

We performed both NEMD and Hugoniot simulations of shock compression along the low index directions (100), (110), and (111) for a range of particle velocities up to 2.5 km/s (\sim 300 GPa). As mentioned above, both EAM models reproduce the mechanical properties of Ta with about the same degree of accuracy, and we find no noticeable differences in the morphology of defects and/or defect densities between these two models. Therefore, unless otherwise specifically noted, the figures in this section, particularly those of defect structures and shock-induced plastic deformation should be taken to correspond to both interatomic models.

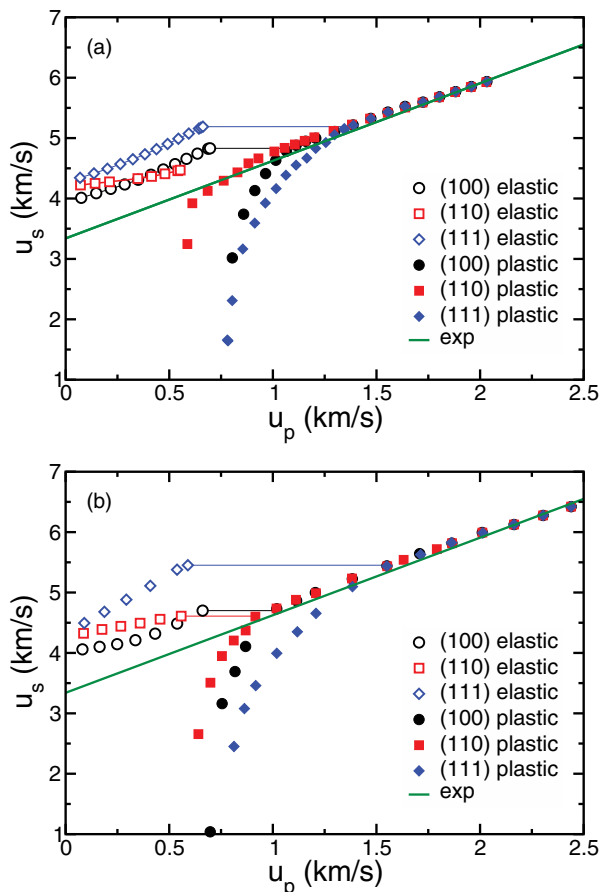


FIG. 8. (Color online) Shock Hugoniot of Ta single crystals for wave propagation along the (100), (110), and (111) crystal directions. Most of the data was evaluated employing the Hugoniotstat method (Ref. 61). Open and closed circles: (100) elastic and plastic, respectively; open and closed squares: (110) elastic and plastic, respectively; open and closed diamonds: (111) elastic and plastic, respectively. The experimental line is a linear fit to experimental shock data from Refs. 54 and 64. The horizontal straight lines are a guide to the eye for the location of the overdriven (OD) point on the Hugoniot as described in the text. (a) Ta1 model. (b) Ta2 model.

Figure 8 shows shock velocity (u_s) vs particle velocity (u_p) of the principal Hugoniot of single crystal Ta for shock propagation along the (100), (110), and (111) directions. The data was computed from Hugoniotstat and NEMD simulations. The solid line is a linear fit to experimental shock data from Refs. 54 and 64. As expected, for defect-free single crystals, all shock directions exhibit high Hugoniot elastic limits (HELs), with elastic-plastic transition strains in the 10%–14% range corresponding to shock pressures in the 40–55 GPa range. Also, all three orientations exhibit two-wave structures characterized by an elastic precursor with soliton-like trains at the front of the elastic wave caused by in-phase “beating” of the atomic planes in the elastic region, followed by a plastic wave whose velocity increases with u_p until it reaches the elastic wave speed at the overdriven (OD) point in the $u_s - u_p$ Hugoniot. Figure 9 shows NEMD particle velocity profiles of shock propagation along the (111) direction for piston velocities $u_p = 1.0, 1.6$ and 2.0 km/s ($P_{zz} = 80, 145$ and 195 GPa, respectively). The profiles have been normalized by the piston velocity for clarity.

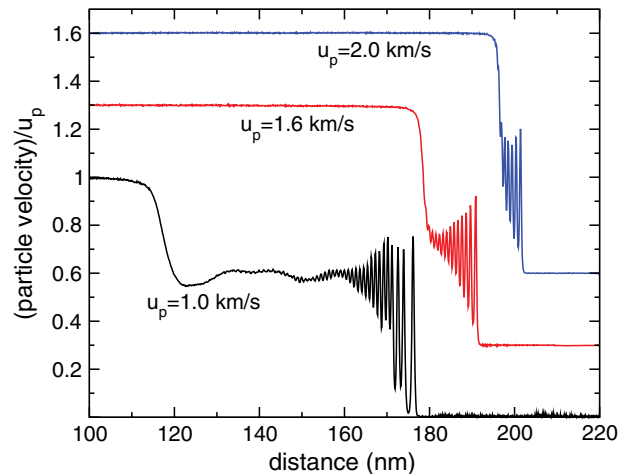


FIG. 9. (Color online) Particle-velocity profiles of shock wave propagation along the (111) orientation for the Ta2 model. The profiles have been shifted and normalized by the corresponding piston velocity for clarity.

It should be noted that the OD shock pressure for this direction is 142 GPa, the highest of the three directions.

For split-waves, the shock velocity of the plastic wave $u_s^{(2)}$ can be written in terms of the particle-velocity, shock pressure and specific volume at the HEL ($u_p^{\text{HEL}}, P_{zz}^{\text{HEL}}, V_{\text{HEL}}$) as

$$u_s^{(2)} = u_p^{\text{HEL}} + \sqrt{\frac{V_{\text{HEL}}(P_{zz}^{(2)} - P_{zz}^{\text{HEL}})}{(1 - V_2/V_{\text{HEL}})}}, \quad (14)$$

where $P_{zz}^{(2)}$ and V_2 are the final shock pressure and specific volume, respectively. For shock pressures above P_{zz}^{HEL} , the system undergoes an elastic-plastic transition characterized by a volume collapse in all three directions and a large increase in temperature due to the enormous dislocation densities (10^{12} – 10^{14} cm $^{-2}$) produced within the plastic zone. The elastic-plastic transition is anisotropic in strain and shear stress, with the (110) orientation exhibiting the lowest shear stress at the HEL (τ_{HEL}), followed by the (100) and (111) directions. The shear stress τ is defined as

$$\tau = \frac{1}{2} [P_{zz} - \frac{1}{2}(P_{xx} + P_{yy})] \quad (15)$$

$$= \frac{3}{4} (P_{zz} - P), \quad (16)$$

where P_{zz} and P are the longitudinal (shock) and volumetric pressure, respectively. The shear stress τ so defined is one-half the von Mises deviatoric stress. The value of τ_{HEL} for the Ta1(Ta2) model is 6(7), 10(9), and 15(18) GPa for the (110), (100) and (111) directions, respectively. Table III summarizes the values of uniaxial strain and shock pressure (longitudinal stress) at the Hugoniot elastic limit (HEL) and overdriven (OD) points of the principal Hugoniot shown in Fig. 8. The values were calculated from Hugoniotstat simulations.

For particle-velocities above the OD point, the profiles are characterized by a single plastic wave with large elastic oscillations at the shock front which do not decay or disappear with shock strength (Fig. 9) and persist up to the shock melt. The $u_s - u_p$ data falls on the experimental line for all three directions with a shock velocity which extrapolates to the bulk sound speed at zero pressure. The directional anisotropy in the

TABLE III. Longitudinal stress (in GPa) and uniaxial (compressive) strain at the Hugoniot elastic limit (HEL) and overdriven (OD) points of principal Hugoniots shown in Fig 8.

Model	Direction	$\varepsilon_{zz}^{\text{HEL}}$	P_{zz}^{HEL}	$\varepsilon_{zz}^{\text{OD}}$	P_{zz}^{OD}
Ta1	(100)	0.14	56	0.22	85
Ta2	(100)	0.13	49	0.21	77
Ta1	(110)	0.12	40	0.19	68
Ta2	(110)	0.12	41	0.20	71
Ta1	(111)	0.13	57	0.26	120
Ta2	(111)	0.11	54	0.28	142

$u_s - u_p$ Hugoniot is also evident in the OD shock pressures, with the (110) orientation having the lowest value and the (111) direction the highest (see Table III).

Figure 10 shows longitudinal and shear stress profiles for shock wave propagation along the (100) and (111) directions at a particle velocity of $u_p = 0.88$ km/s. This value of u_p lies in the split-wave region of the (100) and (111) Hugoniots (Fig. 8). The atomic configurations in the middle frames of Figs. 10(a) and 10(b) show the atoms in a thin 20 Å slice colored according to their local strain. The coloring gradation from dark to light identifies regions of low to high local strain, respectively. The elastic-plastic zone boundary is clearly visible in the strain map and can also be identified by the rapid drop in the profiles of shear stress [bottom frames of Figs. 10(a) and 10(b)]. As mentioned above, the oscillations in front of the elastic precursor are due to “beating” of atomic planes perpendicular to the propagation direction. These elastic oscillations are ubiquitous in all three crystallographic directions studied. The defects associated with the plastic waves are identified employing a centro-symmetric order parameter,^{13,65} and are shown in the top frame of Figs. 10(a) and 10(b). Only defective (non-bcc) atoms are shown. The dislocation density at the lowest sampled piston velocities is about 10^{12} cm⁻² measured at a distance of ~ 100 –200 nm behind the shock front.

The plastic mechanism of stress relaxation at the shock front is markedly different for (110) shocks compared to that of both (100) and (111) shocks. Deformation twinning is the main stress relaxation mechanism in shock wave propagation along (110) for values of u_p below about 1.2 km/s. In order to readily visualize the twins within the shocked crystals, bcc atoms are colored according to their local orientation with respect to the z axis. This is done by evaluating a three-dimensional orientational order parameter whose components represent the “distance” of the orientation of a bcc atom’s four centrosymmetric nearest neighbors with respect to those in ideal (100), (110), and (111) orientations, with respect to a laboratory-fixed reference direction (here taken as the longitudinal shock direction z). The normalized triad of the inverse of these distances ($d_{100}^{-1}, d_{110}^{-1}, d_{111}^{-1}$) are mapped onto an RGB color triangle with the primary colors red, green, and blue at the corners. For digital 8-bit color, the numerical

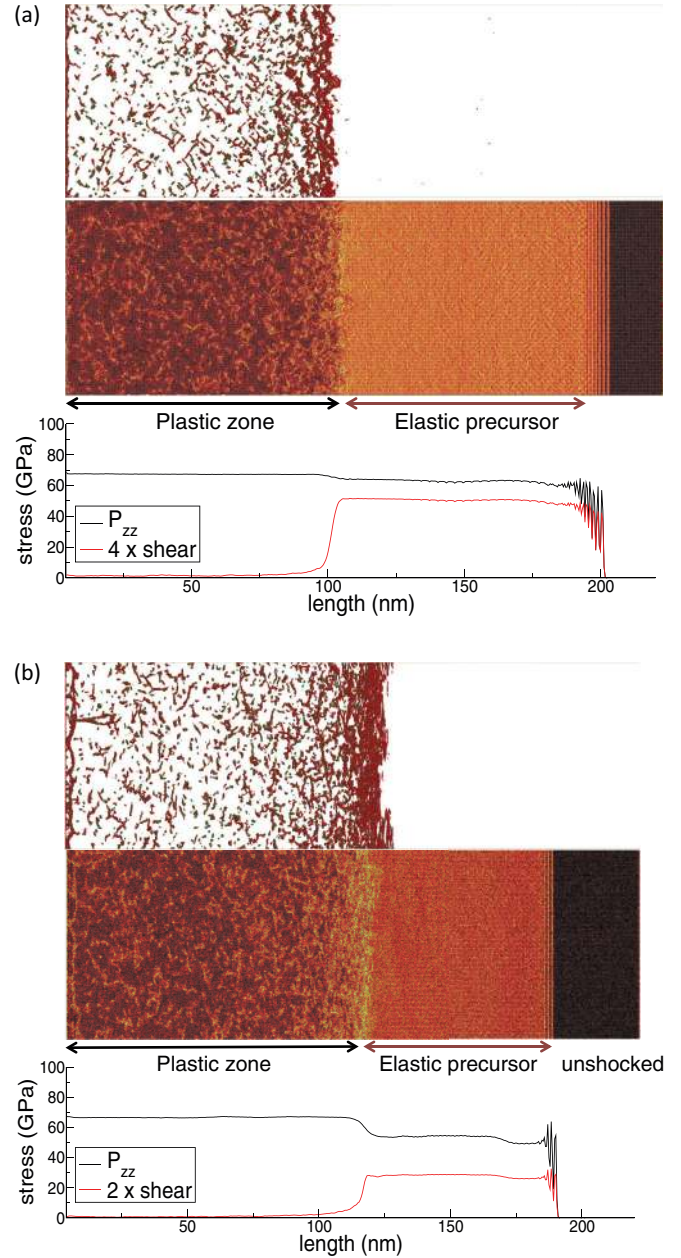


FIG. 10. (Color online) Stress profiles and corresponding atomic configurations of Ta shocked to a particle velocity of $u_p = 0.88$ km/s (~ 67 GPa). (a) Shock wave direction along (100); (b) Shock wave direction along (111). The vertical direction in (b) is along the $\langle 1\bar{1}0 \rangle$. The top and middle frames in both (a) and (b) show the atomic configuration of a thin (20 Å thick) slice. The middle frames in (a) and (b) show atoms colored according to local strain. Darker (lighter) atoms indicate regions of lower (higher) local strain. The top frames in both (a) and (b) show only defective atoms.

representation of this “orientation imaging map” (OIM) vector \mathbf{q}_{oim} , can be expressed as

$$\mathbf{q}_{\text{oim}} = (R, G, B) = \left[\min \left(255, \frac{\sqrt{d_{100}^{-1}}}{d_{\text{norm}}} \right), \min \left(255, \frac{\sqrt{d_{110}^{-1}}}{d_{\text{norm}}} \right), \min \left(255, \frac{\sqrt{d_{111}^{-1}}}{d_{\text{norm}}} \right) \right], \quad (17)$$

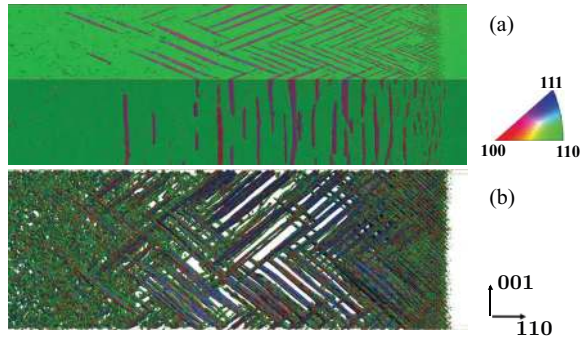


FIG. 11. (Color online) Detailed twin formation pattern in Ta single crystals shocked along (110) to a longitudinal pressure $P_{zz} = 45$ GPa ($u_p = 0.62$ km/s). (a) Atoms colored according to their local orientation with respect to the shock direction (order parameter q_{oim} as defined in the text). (b) Defect structures associated with (a). Only non-bcc atoms are shown.

where $d_{norm} = \sqrt{d_{100}^{-1} + d_{110}^{-1} + d_{111}^{-1}}$. Atoms oriented along (100) have $d_{100} \ll d_{110}, d_{111}$, and are colored with brightest saturated red, while those oriented along (110) and (111) are colored green and blue, respectively. This color-coded orientation mapping is most useful in the visualization and analysis of grains and structural changes in nanocrystal simulations.

Figure 11 shows NEMD simulation results of nucleation and growth of nano-twins in single crystal Ta shocked along (110) to a longitudinal pressure of 45 GPa ($u_p = 0.62$ km/s). The top frame shows a side view of the computational slab with atoms colored according to the OIM order parameter. The Ta (110) computational cell comprised about 64 million atoms arranged in a rectangular slab with a cross sectional area normal to the shock propagation direction of 66×66 nm². Twins nucleate at the shock front and rapidly thicken and grow to an average size of about 40 nm in length. The growth of the nanoscale twins is accompanied by dislocation nucleation and multiplication between twins. This can be seen more clearly in the bottom frame of Fig. 11, which shows a top view of the shocked sample projected along the $\langle 1\bar{1}0 \rangle$ direction (out of the page). Only defective (noncentrosymmetric) atoms are shown.

In order to investigate twin nucleation in more detail, we carried out a series of homogeneous compression simulations employing systems of about $40 \text{ nm} \times 40 \text{ nm} \times 50 \text{ nm}$ (~ 4.4 million atoms) with periodic boundary conditions (PBCs) in all three directions. An affine compressive strain was imposed in the (110) (z) direction while the lateral dimensions were kept at their initial zero pressure, room temperature value. The compressive strain along (110) was varied between 13% and 15%. In all instances, twins nucleated first, followed by dislocation emission between twins. Figure 12 shows a time sequence of twin nucleation in a sample homogeneously compressed along (110) by 13.5% (~ 45 GPa). Only one twin nucleates in a computational cell of this size. The two twin bands in the figure actually corresponds a single band once PBCs are taken into account. In the top sequence, which shows only defective atoms, dislocations nucleate between twin planes on a longer time scale than twin nucleation. The bottom sequence shows atoms colored according to the orientation order parameter q_{oim} . The twin bands thickened in

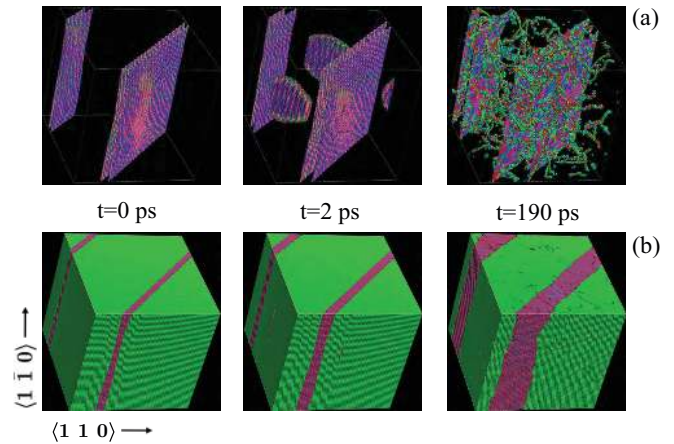


FIG. 12. (Color online) Time snapshots of twin nucleation in Ta compressed homogeneously along (110) by 13.5%. The top sequence shows only defective atoms colored according to a centrosymmetric order parameter. The bottom sequence shows atoms colored according to the OIM order parameter as described in the text. The twins nucleate first, then thicken, followed by dislocation nucleation (Ref. 66).

about the same time scale as in the NEMD simulations for particle-velocities near the HEL. The residual shear stress in the $t = 190$ ps frame is about 5 kbar.

The fact that deformation twinning is observed in shocks along (110) at a lower shear stress values than the elastic-plastic threshold values in (100) and (111) shocks [the shear stress at the HEL in the (110) direction is the lowest of the three] indicates that this is the easiest direction for deformation twinning, perhaps due to a preferred orientation between parent and twin lattices. However, once they are nucleated, dislocation nucleation and multiplication follows, lowering further the residual shear stress. Twin bands continually anneal out behind the shock front in those regions where the shear stress drops below 1.0–1.5 GPa, and as a result, the density of twins decreases sharply with distance from the shock front. Clearly thicker twins are more stable than the minimal two-layer embryos which nucleate at the shock front. However, twins as thick as 20–25 nm anneal out behind the shock front, their growth being arrested once the residual shear stress drops below 1 GPa. The interplay between the growth rate and an “effective” shear stress zone, provides a measure of the width of the deformation twinning zone and how far from the shock front twins can thicken and grow. The twinning zone shrinks with increasing particle-velocity, as the width of the shear stress profile decrease with increasing shock pressure. Above particle-velocities of about 1.2 km/s (~ 100 GPa), twin embryos nucleate at the shock front but do not grow, and the number of twins in the shocked samples is very much reduced. Figure 13 shows snapshots from NEMD simulations of (110) shock wave propagation in Ta at three different particle velocities (shock pressures): $u_p = 0.60$ km/s (43 GPa), 0.80 km/s (62 GPa), and 1.20 km/s (~ 100 GPa). Atoms are colored according to the OIM order parameter. At the highest pressure (100 GPa), the morphology and density of defects agrees with what is observed in (100) and (111) shocks at about the same pressure. It is clear that deformation twinning is considerably

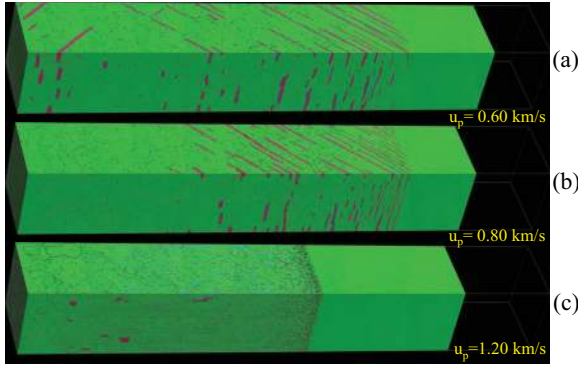


FIG. 13. (Color online) Shock-induced twinning in Ta single crystal shocked along (110) at various particle velocities employing the Ta1 model: (a) $u_p = 0.60$ km/s; (b) $u_p = 0.80$ km/s; (c) $u_p = 1.20$ km/s. Atoms are colored according to orientation order parameter q_{0im} as described in the text. Twin formation is clearly visible for $u_p = 0.60$ and 0.80 km/s.

more pronounced in (110) shocks as compared to (100) and (111) directions. This is also the observed trend in recent gas gun recovery experiments of Ta single crystals shocked to 25 and 55 GPa. In those experiments, the (110) samples were found to have the largest amount of twins at 55 GPa compared to the (100) and (111) samples at the same pressure.⁶⁷

A. Directional dependence of the flow stress

The particle-velocity and stress profiles can be used to deduce the flow stress as a function of volumetric strain. NEMD shockwave simulations provide a direct way of computing the strain rate from the spatial derivative of the particle-velocity profile as well as the deviatoric stress and volumetric strain through the shock path. In the elastic-plastic regime of the Hugoniot, the maximum shear stress $\tau_{\max} = \tau_{\text{HEL}}$ for plastic wave speeds below the overdriven point. The elastic oscillations in the particle velocity and shear stress profiles makes it difficult to continuously determine the strain rate through the shock path. However, estimates of the flow stress and plastic strain rate can be made by computing averages of these quantities in the plastic zone. The procedure employed in evaluating these averages was slightly modified to deal with split-wave profiles.

Estimates of the flow stress and plastic strain rate in the two-wave regime were made by computing averages of these quantities over a plastic flow region defined from the leading edge of the plastic wave (Z_1) to a point Z_2 along the shock path where $u_p(z)$ reaches 98% of its steady-state value (see Fig. 9). For overdriven shocks, plastic flow was assumed to commence at the middle of the shock where the shear stress is a maximum. Thus, OD averages were computed in the region between the middle of the shock and Z_2 :

$$\langle \dot{\epsilon} \rangle = \frac{1}{\lambda} \int_{Z_1}^{Z_2} \dot{\epsilon}(z) dz \quad (18)$$

$$= \frac{[u_p(Z_2) - u_p(Z_1)]}{\lambda}, \quad (19)$$

$$\langle \tau \rangle = \frac{1}{\lambda} \int_{Z_1}^{Z_2} \tau(z) dz, \quad (20)$$

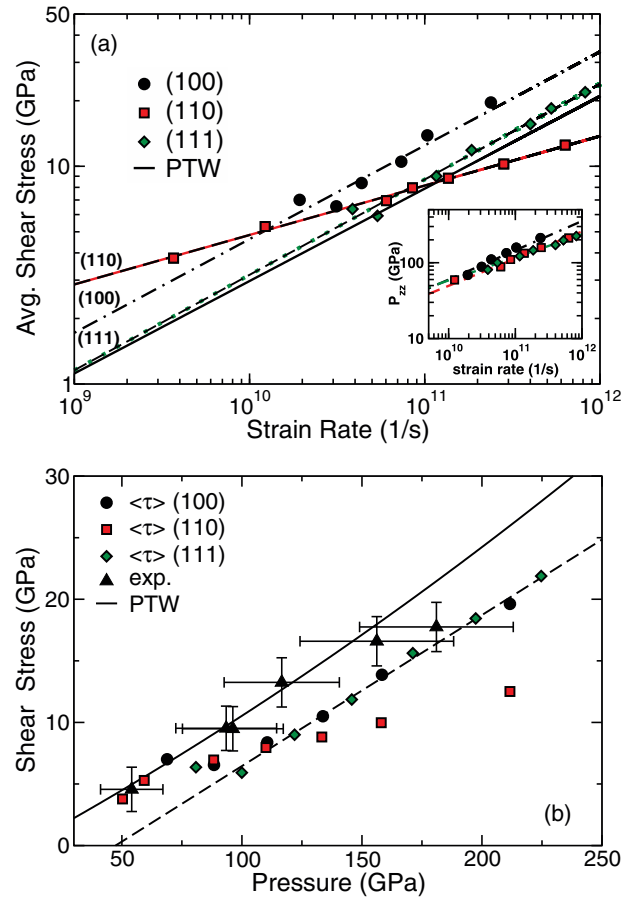


FIG. 14. (Color online) (a) Average plastic shear stress vs. average strain rate as a function of shock direction. The dashed lines are power-law fits to the NEMD data with exponents 0.43, 0.23, and 0.44 for (100), (110), and (111), respectively. The solid black line is the prediction from the Preston-Tonks-Wallace (PTW) strength model (Ref. 68). Inset: longitudinal shock pressure vs average plastic strain rate. The dashed lines are power fits of the form $P_{zz} = A\dot{\epsilon}^\alpha$, with the exponent $\alpha = 0.39, 0.36, 0.30$ for (100), (110), and (111), respectively. (b) Average shear stress vs pressure for the three low index directions (100) (circles), (110) (squares), and (111) (diamonds). The dashed line going through the (100) and (111) $\langle \tau \rangle$ data is a guide to the eye. The solid black line is the prediction from the Preston-Tonks-Wallace (PTW) strength model (Ref. 68). The experimental data (solid triangles) are from Ref. 71, and correspond to single-crystal Ta shocked along (100).

where the shear stress τ is given by (15) and the width $\lambda = Z_2 - Z_1$ is approximately one-half the effective width of the shock. Along with the average flow stress and average strain rate, other quantities computed from the NEMD profiles included maximum shear stress, maximum strain rate, uniaxial strain, and the stress and temperature tensors.

The average shear stress versus average strain rate so computed is shown in Fig. 14(a) for the (100), (110), and (111) directions. The data was fitted to a power law in strain rate (dashed lines) with exponents 0.43, 0.23, and 0.44 for the (100), (110), and (111) directions respectively. Also shown is the prediction of the Preston-Tonks-Wallace (PTW) strength model⁶⁸ for the average flow stress vs average plastic strain rate (solid line). The model's flow stress also follows

a power law in plastic strain rate with exponent 0.424, very close to the strain-rate dependence of the (100) and (111) NEMD data. It should be pointed out that the PTW data have been un-normalized by the model's shear modulus $G(\varepsilon, T)$. Normalizing both the NEMD (100) and (111) average shear stress data as well as the PTW flow stress by the appropriate (directional or isotropic) pressure- and temperature-dependent shear moduli yields a power exponent in strain rate close to 1/4. However, this 1/4 power dependence is not related to the often-quoted Swegle-Grady (S-G) relation between the shock pressure and the total strain rate.⁶⁹ The S-G relation does not seem to hold at the very high strain rates attained in shocked single crystals. The inset in Fig. 14(a) shows NEMD shock pressures vs average strain rate for the three sampled directions. The data can be fitted to a power law in strain rate, $P_{zz} = (\dot{\varepsilon})^\alpha$ with the exponent $\alpha = 0.39, 0.36,$ and 0.30 for the (100), (110), and (111) directions, respectively. The NEMD shock pressures clearly follow a higher power dependence in strain rate than 1/4, the S-G value which is known to be applicable at lower strain rates (10^5 – 10^7 s⁻¹). NEMD studies of shock strength in both defective and defect-free Cu single crystals also find that at high strain rates the dependence of the shock pressure with strain rate follows a power law with an exponent close to 0.40.⁷⁰

We can conclude that the dynamical strength of single crystal Ta is anisotropic, with compression along the (100) and (111) orientations exhibiting higher average shear stress values than compression along (110). This difference grows with pressure (or strain rate), and at 200 GPa, the calculated average flow stress is 12 GPa for (110) and 18.5 GPa for (100) and (111). The maximum shear stress difference between these orientations follows a similar ratio as the average values. The average shear stress as a function of pressure for all three directions is shown in Fig. 14(b) where we compare the NEMD results with recent experiments of laser shocked single crystal Ta along (100)⁷¹ and the theoretical prediction of the PTW strength model.⁶⁸

The lower strain-rate dependence of the flow stress in the (110) direction can be understood from the observed deformation twinning, the main mechanism of stress relief at the shock front in this direction. Twin nucleation occurs at faster rates than dislocation nucleation, which proceeds subsequently to twin nucleation and growth. This results in lower shear stress maxima for this direction, and, as a consequence, dislocation nucleation in shocked Ta(110) progresses at nominally lower shear stress than in (100) or (111) directions. This is similar to the directional anisotropy found in the mechanical strength of fcc single crystals, where faster partial loop nucleation is the main mechanism of stress relief for shock wave propagation along (100), rather than the slower full loop nucleation observed for propagation along the (110) or (111) directions.^{12,13}

B. Hugoniot temperatures

We examined shock temperature as a function of shock pressure and orientation, in order to investigate what (if any) role defect morphology and microstructure might play on Hugoniot temperatures. While polycrystalline and microstructure effects are expected to be minimal in shock velocities,

different dissipation mechanisms can influence shock width and rise times as well as strain rates, and shock temperatures should be more sensitive to these effects. In single-crystal Ta, stress relief along (110) is different from (100) and (111), due primarily to twin nucleation at the shock front. Furthermore, the maximum deviatoric stress in this direction is the lowest of the three orientations for reasons that have been outlined above. Thus, if defect microstructure and evolution play a role in the shock temperature, we would anticipate these differences to be more pronounced between (110) and both (111) and (100) directions. As we detail below, we find this is not the case in Ta single crystals.

Most of the data presented here were collected with the Ta2 model, given that it more accurately accounts for thermal pressures than the Ta1 model (see Table II). The equilibrium melt curve of the Ta models was determined from solid-liquid coexistence simulations⁵⁸ employing rectangular slabs comprising 16 000 atoms and periodic boundary conditions (PBC) in all directions. The pressure was varied from 0–380 GPa for the Ta1 model and 0–280 GPa for the Ta2 model, and the results were fitted with the Simon equation, $T_m(P) = T_0(1 + P/\alpha)^\beta$, where $T_0 = 3033$ K, $\alpha = 19.137$ GPa, and $\beta = 0.158$ for the Ta1 model (with 3080 K, 24.774 GPa, and 0.342, respectively, for the Ta2 model). The melt curve of the Ta2 model is shown in Fig. 15 along with DAC melting data and other theoretical results. The calculated equilibrium melt line, while in good agreement with recent DAC melt data,⁷ differs from DFT-based free energy calculations²⁹ (open circles), and this difference increases with pressure. The Ta1 model melt curve, while in better agreement with the experimental DAC data of Errandonea *et al.*,⁴ underestimates significantly the melt line at high pressures when compared to theoretical DFT calculations.

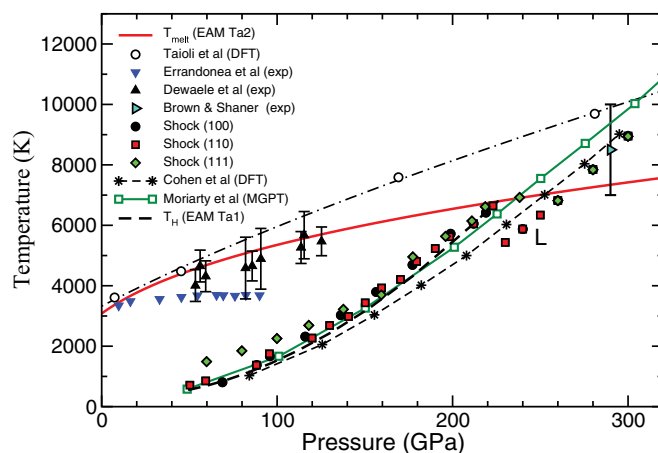


FIG. 15. (Color online) Melt curve and Hugoniot temperatures calculated with the Ta2 model (solid line and solid circles, squares, and diamonds) compared with experimental melt data (down triangles: Ref. 5; up triangles: Ref. 7); and the melt curve from DFT calculations (open circles: Ref. 29). Also shown are theoretical calculations of the Hugoniot temperature (stars: Ref. 52; open squares: Ref. 9); together with an estimate of the Hugoniot temperature with the Ta1 model (dashed line) using an isotropic EOS and treating the thermal pressure within the quasiharmonic approximation for the Rankine-Hugoniot condition as described in the text.

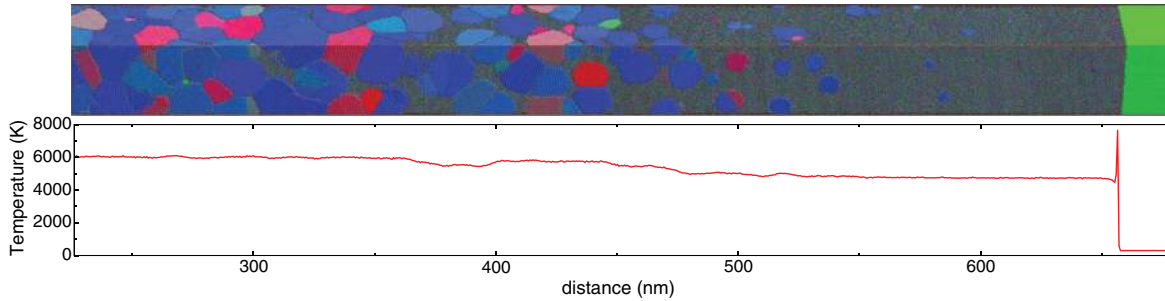


FIG. 16. (Color online) Top: atomic configuration in a 450 nm section of a 1-micron-long NEMD simulation of single-crystal Ta (110) shocked to a pressure of 212 GPa using the Ta2 model. The atoms are colored according to the OIM order parameter [Eq. (17)]. The material at the shock front is a cold liquid which recrystallizes into a completely isotropic nanocrystal sample. The nanograins are colored accordingly to their local orientation with respect to the shock direction (orientation color map shown in Fig. 11). Bottom: temperature profile in atomic region shown on top figure. The shock temperatures are 4750 K and 6050 K in the liquid and solid regions, respectively.

The pressure-temperature Hugoniots from NEMD and Hugoniot simulations are shown in Fig. 15 along with theoretical calculations by Cohen and Güleren⁵² and Moriarty *et al.*⁹ The single crystal shock temperatures are anisotropic in the elastic-plastic region with the (111) direction exhibiting higher temperatures by as much as 600 K compared to the (100) and (110) orientations. This is due primarily to the anisotropy of the HEL with shock direction and the large difference in volume collapse at the elastic-plastic transition between the (111) orientation (7.4%) and the (100) and (110) orientations ($\sim 4\%$). This volume difference provides additional P - V work ($\sim P_{\text{HEL}} \Delta V$), which results in a larger internal energy change in the Rankine-Hugoniot conditions. Above the overdriven pressure, the Hugoniot temperature is independent of orientation, and the Ta2 model predicts a shock melt pressure of 220 GPa for all three directions, which is lower than the experimental estimate of 290 GPa.³⁸ The pressure dependences of the (100) and (110) Hugoniot temperatures of both EAM models are in close agreement with the MGPT model calculations for Ta of Moriarty *et al.*⁹ for pressures below about 180 GPa, but are steeper than the DFT results of Cohen and Güleren.⁵² We do not believe the difference with the DFT results is due to electron-thermal contributions, at least not at these pressures.⁷² It also cannot be attributed to differences in the Grüneisen parameter, whose DFT calculations overestimate and the EAM models presented here underestimate at zero pressure. We find that the EAM model (Ta1) with the lowest estimate of the zero-pressure Grüneisen parameter also predicts higher Hugoniot pressures at fixed temperature, opposite to what one would expect. We thus conclude that the pressure dependence of the Hugoniot temperature of Ta is not strongly dependent on the zero-pressure value(s) of the vibrational Grüneisen parameter, Eq. (10).

Employing the EAM models' EOS, we evaluated the P-T Hugoniot curve by solving the Rankine-Hugoniot equation,

$$E(V, T) = E_0(V_0, T_0) + \frac{1}{2} P(V, T) [V_0(T_0) - V], \quad (21)$$

treating the thermal pressure within the quasiharmonic approximation and ignoring directional anisotropy. Calculating the Hugoniot this way gives results that agree well with NEMD simulations in the OD region, indicating that the Mie-Grüneisen (M-G) formalism works well for this system for

pressures below 200 GPa, and that plasticity and material inhomogeneities play no significant role in shock temperatures.

For pressures above about 180 GPa, the NEMD shock temperatures show a larger increase with pressure compared with the isotropic calculations based on the Mie-Grüneisen formulation, as well as with the theoretical results of Moriarty *et al.*⁹ Upon further inspection, we find that above this pressure, the material at the shock front premelts at a temperature much below the equilibrium melt temperature. A metastable liquid zone forms behind the shock, subsequently recrystallizing into an isotropic, nanocrystalline state at a rate inversely proportional to the difference between the shock front temperature and the equilibrium melt temperature at the corresponding pressure. This premelting phenomenon has been observed by several authors in simulations of directional melting in fcc single crystals.^{73–76} However, unlike fcc crystals where only the (110) and (111) directions exhibit premelting and the (100) orientation exhibits overheating, here the shocked crystal premelts in all three directions at about the same pressure-temperature point in the Hugoniot. The thickness of the metastable liquid region behind the shock increases with shock temperature and/or pressure. This necessitates NEMD simulations with computational cells of a micron or longer in length in order to fully capture the recrystallization process. Figure 16 shows the atomic configuration and temperature profile in a 450 nm section of a 1-micron-long NEMD simulation of Ta shocked along the (110) direction at a piston velocity of 2.10 km/s (210 GPa). The liquid zone, at a temperature of 4750 K, extends for about 150 nm behind the shock front. It recrystallizes into a nanocrystal at a steady-state temperature of 6050 K. The premelting is not an artifact of the simulations or the models, but rather is due to the very large strain rates at these pressures that produce elastic deformations of $\sim 30\%$ or higher. Quasi-isentropic compression simulations to the same pressures, but at much lower strain rates ($\sim 10^9 \text{ s}^{-1}$), yield defective states with no signs of premelt.

V. SUMMARY AND CONCLUSIONS

Using NEMD, we have studied the plastic deformation mechanisms in shock-wave compression of single-crystal tantalum for different propagation directions along the low

index directions (100), (110), and (111). As part of this study, we developed two new EAM interatomic potentials of Ta, optimized by fitting to a database of DFT and experimental data. From the onset, it was not clear how well a simple EAM model could reproduce the mechanical properties of bcc metals at compressions relevant to shock-wave experiments. The models presented here do surprisingly well over the sampled pressure range. We found that it was necessary to incorporate into the fitting routines the enthalpy differences between bcc and other energetically close phases, in order to eliminate artificial phase transitions with pressure.

As expected for single crystals, the Hugoniot elastic limit (HEL) of all three orientations is high (40–50 GPa), with the (110) orientation having the lowest value and (111) the highest. All three principal Hugoniot exhibit a split-wave region; for shock waves along the (111) direction, this region extends to very high pressures (120–140 GPa).

We find that deformation twinning is the main mechanism of stress relaxation in (110) shocks for piston velocities below about 1.2 km/s (~ 100 GPa). Above this, twin embryos nucleate at the shock front but do not grow, and the number of twins in the shocked samples is very much reduced. Also, deformation twinning is significantly more pronounced in shocks along (110), compared to the (100) and (111) directions. The twinning stress threshold can be reduced by preexisting defects. Studies of shock wave compression in defective Ta (100) monocrystals employing the Ta1 EAM model of this work estimate the twinning threshold to be between 25 and 35 GPa.⁷⁷ However, the twin volume fraction along (100) is significantly lower when compared to (110). This trend has also been observed in recent gas gun recovery experiments of Ta single crystals.⁶⁷ We anticipate this will also be the case for (111) shocks for which a more detailed defect analysis remains to be done.

From the particle-velocity and shear stress profiles along the shock path, we computed averages of the flow stress and strain rate in the plastic flow region, defined to be from the middle of the shock to the point in the shock path where the particle velocity reaches 98% of the piston velocity. The strain-rate dependence of the average flow stress follows a power law of the form $\langle \tau \rangle = A \langle \dot{\epsilon} \rangle^\alpha$, where the exponent $\alpha = 0.43, 0.23,$ and 0.44 for (100), (110), and (111) orientations, respectively, for strain rates between 10^9 and 10^{12} s⁻¹. The weaker dependence of the (110) direction can be explained from the observed deformation twinning, where twin nucleation occurs at a faster rate than dislocation nucleation. As a result, dislocation nucleation occurs at lower shear stress values in (110) than for (100) or (111), resulting in lower dislocation densities for (110). This is also consistent with

significantly lower maximum values of shear stress in (110) than in (100) or (111). The pressure dependence of the average flow stress for the (100) and (111) directions is in agreement with recent laser shock experiments of Ta (100).⁷¹ We also find the pressure and strain-rate dependence of the flow stress computed from the simulations are in excellent agreement with the Preston-Tonks-Wallace (PTW) strength model for Ta in the overdriven shock regime.⁶⁸

Finally, we examined shock temperatures of the Ta models for different orientations. The main goal of this part of our study was to investigate the effect of defect morphology and single-crystal plasticity on the Hugoniot temperature. We found that (111) shock temperatures are higher than (100) and (110) for pressures below the overdriven pressure. This result is consistent with a higher HEL in (111) and also a higher volume collapse of the elastic-plastic transition. Above the OD point, the shock temperature for all three directions is independent of orientation. This result was surprising, given the very different mechanisms of plastic relief at the shock front in the (110) direction (twinning) compared to (100) and (111). This could suggest that shock temperatures are insensitive in the overdriven regime to the underlying microstructure. However, we find pronounced differences in the temperature profiles in the two-wave region of the Hugoniot. The time scale over which the temperature profiles approach the steady state might provide a measure of the mean relaxation times of the anisotropic plastic flow in single crystal plasticity. Overall, the NEMD single-crystal shock temperatures at a fixed pressure are higher than DFT calculations of the principal Hugoniot, where the thermal pressure is computed in the quasi-harmonic approximation. A similar calculation, employing our model potentials, produces temperatures which are in very good agreement with the (100) and (110) NEMD shock temperatures, in spite of the different values between the vibrational and thermodynamic Grüneisen in these two EAM models.

ACKNOWLEDGMENTS

The authors would like to thank Jonathan Boettger, James E. Hammerberg, and Davis Tonks for useful discussions and valuable comments. Work at Los Alamos was performed under the auspices of the U.S. Department of Energy (DOE) under Contract No. DE-AC52-06NA25396 and was supported by the Laboratory Directed Research and Development program. R. R. acknowledges support from the Air Force Office of Scientific Research under AFOSR Award No. FA9550-12-1-0476.

*Corresponding author: ravelo@utep.edu

†tcg@lanl.gov

‡oguerrero@miners.utep.edu

§anqi@caltech.edu

||blh@lanl.gov

¹L. M. Hsiung and D. H. Lassila, *Acta Mater.* **48**, 4851 (2000).

²L. Burakovsky, S. P. Chen, D. L. Preston, A. B. Belonoshko, A. Rosengren, A. S. Mikhaylushkin, S. I. Simak, and J. A. Moriarty, *Phys. Rev. Lett.* **104**, 255702 (2010).

³J. B. Haskins, J. A. Moriarty, and R. Q. Hood, *Phys. Rev. B* **86**, 224104 (2012).

⁴D. Errandonea, B. Schwager, R. Ditz, C. Gessmann, R. Boehler, and M. Ross, *Phys. Rev. B* **63**, 132104 (2001).

- ⁵D. Errandonea, M. Somayazulu, D. Häusermann, and H. K. Mao, *J. Phys.: Condens. Matter* **15**, 7635 (2003).
- ⁶J. Ruiz-Fuertes, A. Karandikar, R. Boehler, and D. Errandonea, *Phys. Earth Planet. In.* **145**, 69 (2010).
- ⁷A. Dewaele, M. Mezouar, N. Guignot, and P. Loubeyre, *Phys. Rev. Lett.* **104**, 255701 (2010).
- ⁸L. L. Hsiung, *J. Phys.: Condens. Matter* **22**, 385702 (2010).
- ⁹J. A. Moriarty, J. F. Belak, R. E. Rudd, P. Söderlind, F. H. Streitz, and L. H. Yang, *J. Phys.: Condens. Matter* **14**, 2825 (2002), and references therein.
- ¹⁰D. S. Orlikowski, P. Söderlind, and J. A. Moriarty, *Phys. Rev. B* **74**, 054109 (2006), and references therein.
- ¹¹M. Foata-Prestavoine, G. Robert, M.-H. Nadal, and S. Bernard, *Phys. Rev. B* **76**, 104104 (2007), and references therein.
- ¹²T. C. Germann, B. L. Holian, P. S. Lomdahl, and R. Ravelo, *Phys. Rev. Lett.* **84**, 5351 (2000).
- ¹³T. C. Germann, D. Tanguy, B. L. Holian, P. S. Lomdahl, M. Mareschal, and R. Ravelo, *Metall. Mater. Trans. A* **35**, 2609 (2004).
- ¹⁴R. F. Zhang, J. Wang, I. J. Beyerlein, and T. C. Germann, *Philos. Mag. Lett.* **91**, 731 (2011).
- ¹⁵V. Vitek, *Phil. Mag.* **84**, 415 (2004).
- ¹⁶A. Seeger and W. Wasserbach, *Phys. Status Solidi A* **189**, 27 (2002).
- ¹⁷R. A. Johnson and D. J. Oh, *J. Mater. Res.* **4**, 1195 (1989).
- ¹⁸A. M. Guellil and J. B. Adams, *J. Mater. Res.* **7**, 639 (1992).
- ¹⁹M. W. Finnis and J. E. Sinclair, *Philos. Mag. A* **50**, 45 (1984).
- ²⁰G. J. Ackland and R. Thetford, *Philos. Mag. A* **56**, 15 (1987).
- ²¹X. D. Dai, Y. Kong, J. H. Li, and B. X. Liu, *J. Phys.: Condens. Matter* **18**, 4527 (2006).
- ²²Z. L. Liu, L. C. Cai, X. R. Chen, and F. Q. Jing, *Phys. Rev. B* **77**, 024103 (2008).
- ²³B. J. Lee, M. I. Baskes, H. Kim, and Y. K. Cho, *Phys. Rev. B* **64**, 184102 (2001).
- ²⁴Y. Mishin and A. Y. Lozovoi, *Acta Mater.* **54**, 5013 (2006).
- ²⁵J. A. Moriarty, L. X. Benedict, J. N. Glosli, R. Q. Hood, D. A. Orlikowski, M. V. Patel, P. Söderlind, F. H. Streitz, M. Tang, and L. H. Yang, *J. Mater. Res.* **21**, 563 (2006).
- ²⁶G. Kresse and J. Hafner, *Phys. Rev. B* **47**, 558 (1993); **49**, 14251 (1994); G. Kresse and J. Furthmüller, *Comput. Mater. Sci.* **6**, 16 (1996); *Phys. Rev. B* **54**, 11169 (1996).
- ²⁷P. E. Blochl, *Phys. Rev. B* **50**, 17953 (1994).
- ²⁸J. P. Perdew, in *Electronic Structure of Solids '91*, edited by P. Ziesche and H. Eschrig (Akademie-Verlag, Berlin, 1991); J. P. Perdew, J. A. Chevary, S. H. Vosko, K. A. Jackson, M. R. Pederson, D. J. Singh, and C. Fiolhais, *Phys. Rev. B* **46**, 6671 (1992).
- ²⁹S. Taioli, C. Cazorla, M. J. Gillan, and D. Alfe, *Phys. Rev. B* **75**, 214103 (2007).
- ³⁰J. C. Boettger, *Phys. Rev. B* **64**, 035103 (2001).
- ³¹H. J. Monkhorst and J. D. Pack, *Phys. Rev. B* **13**, 5188 (1976).
- ³²M. S. Daw and M. I. Baskes, *Phys. Rev. B* **29**, 6443 (1984).
- ³³A. F. Voter, in *Intermetallic Compounds: Principles and Practice*, edited by J. H. Westbrook and R. L. Fleischer (John Wiley and Sons, New York, 1993).
- ³⁴R. Ryberg, *Z. Phys.* **73**, 376 (1932).
- ³⁵J. H. Rose, J. R. Smith, F. Guinea, and J. Ferrante, *Phys. Rev. B* **29**, 2963 (1984).
- ³⁶F. Guinea, J. R. Smith, J. H. Rose, and J. Ferrante, *Appl. Phys. Lett.* **44**, 53 (1984).
- ³⁷B. L. Holian, A. F. Voter, N. J. Wagner, R. J. Ravelo, S. P. Chen, W. G. Hoover, C. G. Hoover, J. E. Hammerberg, and T. D. Dontje, *Phys. Rev. A* **43**, 2655 (1991).
- ³⁸J. M. Brown and J. W. Shaner, in *Shock Waves in Condensed Matter*, edited by J. R. Asay, R. A. Graham, and G. K. Straub (Elsevier, New York, 1984).
- ³⁹A. Corana, M. Marchesi, C. Martini, and S. Ridella, *ACM Trans. Math. Software* **13**, 262 (1987).
- ⁴⁰A. Dewaele, P. Loubeyre, and M. Mezouar, *Phys. Rev. B* **70**, 094112 (2004).
- ⁴¹F. R. de Boer, R. Boom, W. C. M. Mattens, A. R. Miedema, and A. K. Niessen, *Cohesion in Metals: Transition Metal Alloys* (Elsevier Scientific, New York, 1988).
- ⁴²W. L. Stewart, J. M. Roberts, N. G. Alexandropolous, and K. Salama, *J. Appl. Phys.* **48**, 75 (1977).
- ⁴³H. Cynn and C. S. Yoo, *Phys. Rev. B* **59**, 8526 (1999).
- ⁴⁴P. Söderlind and J. A. Moriarty, *Phys. Rev. B* **57**, 10340 (1998).
- ⁴⁵K. Maier, M. Peo, B. Saile, H. E. Schaefer, and A. Seeger, *Philos. Mag. A* **40**, 701 (1979).
- ⁴⁶A. Satta, F. Willaime, and S. de Gironcoli, *Phys. Rev. B* **60**, 7001 (1999).
- ⁴⁷H. Schultz and P. Ehrhart, *Atomic Defects in Metals, New Series, Group III* (Springer, Berlin, 1991).
- ⁴⁸W. R. Tyson and W. A. Miller, *Surf. Sci.* **62**, 267 (1977).
- ⁴⁹A. Kiejna, *Surf. Sci.* **598**, 276 (2005).
- ⁵⁰R. E. Bedford, G. Bonnier, H. Maas, and F. Pavese, *Metrologia* **33**, 133 (1996).
- ⁵¹*ASM Ready Reference: Thermal Properties of Metals*, edited by F. Cverna (ASM International, Materials Park, OH, 2002).
- ⁵²R. E. Cohen and O. Gülseren, *Phys. Rev. B* **63**, 224101 (2001).
- ⁵³W. Katahara, M. H. Maghni, and E. S. Fisher, *J. Phys. F* **9**, 773 (1979).
- ⁵⁴S. P. Marsh, *LASL Shock Hugoniot Data* (University of California Press, Berkeley 1980).
- ⁵⁵J. S. Dugdale and D. K. C. MacDonald, *Phys. Rev.* **89**, 832 (1953).
- ⁵⁶O. L. Anderson, *Geophys. J. Int.* **143**, 279 (2000), and references therein.
- ⁵⁷R. Ravelo and B. L. Holian (unpublished).
- ⁵⁸J. R. Morris, C. Z. Wang, K. M. Ho, and C. T. Chan, *Phys. Rev. B* **49**, 3109 (1994).
- ⁵⁹M. de Podesta, *Understanding the Properties of Matter*, 2nd ed. (Taylor & Francis, London, 2002).
- ⁶⁰A. T. Paxton, P. Gumbsch, and M. Methfessel, *Philos. Mag. Lett.* **63**, 267 (1991).
- ⁶¹R. Ravelo, B. L. Holian, T. C. Germann, and P. S. Lomdahl, *Phys. Rev. B* **70**, 014103 (2004).
- ⁶²P. S. Lomdahl, P. Tamayo, N. Grønbech-Jensen, and D. M. Beazley, in *Proceedings of Supercomputing '93* (IEEE, Piscataway, NJ, 1993), p. 520; K. Kadau, T. C. Germann, and P. S. Lomdahl, *Int. J. Mod. Phys. C* **17**, 1755 (2006).
- ⁶³B. L. Holian and P. S. Lomdahl, *Science* **80**, 2085 (1998).
- ⁶⁴A. C. Mitchell and W. J. Nellis, *J. Appl. Phys.* **52**, 3363 (1981).
- ⁶⁵C. L. Kelchner, S. J. Plimpton, and J. C. Hamilton, *Phys. Rev. B* **58**, 11085 (1998).
- ⁶⁶See Supplemental Material at <http://link.aps.org/supplemental/10.1103/PhysRevB.88.134101> for movie of homogeneous twin nucleation in tantalum uniaxially compressed along the (110) direction.
- ⁶⁷J. N. Florando, N. R. Barton, B. S. El-Dasher, J. M. McNaney, and M. Kumar, *J. Appl. Phys.* **113**, 083522 (2013).

- ⁶⁸D. L. Preston, D. L. Tonks, and D. C. Wallace, *J. Appl. Phys.* **93**, 211 (2003).
- ⁶⁹J. W. Swegle and D. E. Grady, *J. Appl. Phys.* **58**, 695 (1985).
- ⁷⁰R. Ravelo, B. L. Holian, and T. C. Germann, in *Shock Compression of Condensed Matter 2009*, Proceedings of the American Physical Society Topical Group, Nashville, edited by M. Elert, M. D. Furnish, W. W. Anderson, W. G. Proud, and W. T. Butler, AIP Conf. Proc. No. 1195 (AIP, New York, 2009), p. 825.
- ⁷¹A. J. Comley, B. R. Maddox, R. E. Rudd, S. T. Prisbrey, J. A. Hawreliak, D. A. Orlikowski, S. C. Peterson, J. H. Satcher, A. J. Elsholz, H.-S. Park, B. A. Remington, N. Bazin, J. M. Foster, P. Graham, N. Park, P. A. Rosen, S. R. Rothman, A. Higginbotham, M. Suggit, and J. S. Wark, *Phys. Rev. Lett.* **110**, 115501 (2013).
- ⁷²Studies of shock wave temperatures in aluminum using two-temperature model molecular dynamics (TTM-MD), a method which incorporates the electronic heat conduction and electron-phonon coupling, have shown that differences in shock temperatures between classical MD and TTM-MD treatments are very small: D. S. Ivanov, L. V. Zhigilei, E. M. Bringa, M. De Koning, B. A. Remington, M. J. Caturla, and S. M. Pollaine, in *Shock Compression of Condensed Matter 2003*, Proceedings of the American Physical Society Topical Group, Portland, edited by M. D. Furnish, Y. M. Gupta, and J. W. Forbes, AIP Conf. Proc. No. 706 (AIP, New York, 2004), p. 225.
- ⁷³R. Ravelo, T. C. Germann, B. L. Holian, and P. S. Lomdahl, in *Shock Compression of Condensed Matter 2005*, Proceedings of the American Physical Society Topical Group, Baltimore, edited by M. D. Furnish, M. Elert, T. P. Russell, and C. T. White, AIP Conf. Proc. No. 845 (AIP, New York, 2006), p. 270.
- ⁷⁴Q. An, S. N. Luo, L. B. Han, L. Q. Zheng, and O. Tschauner, *J. Phys.: Condens. Matter* **20**, 095220 (2008).
- ⁷⁵V. I. Levitas and R. Ravelo, *Proc. Natl. Acad. Sci. U.S.A.* **109**, 13204 (2012).
- ⁷⁶M. M. Budzevich, V. V. Zhakhovsky, C. T. White, and I. I. Oleynik, *Phys. Rev. Lett.* **109**, 125505 (2012).
- ⁷⁷D. R. Tramontina, P. Erhart, T. C. Germann, J. A. Hawreliak, A. Higginbotham, N. Park, R. Ravelo, A. Stukowski, M. J. Suggit, Y. Tang, J. S. Wark, and E. M. Bringa (unpublished).